Methods for Dynamic SPECT Tomography

Jean Maeght†, Dominikus Noll†, Anna Celler§ *Member, IEEE*, Troy Farncombe¶
† Université Paul Sabatier, Mathématiques pour l'Industrie et la Physique, 118 route de Narbonne, 31062 Toulouse, France
§ Vancouver Hospital and Health Center, Division of Nuclear Medicine, Vancouver, BC, Canada, V5Z 1M9
¶ University of British Columbia, Physics Department, Vancouver, BC, V6T 1Z1, Canada

Abstract

We present several new reconstruction methods for Single Photon Emission Computed Tomography with dynamic sources. Our approach provides dynamic reconstructions for practically any camera system, including rotating single, double and triple head cameras doing slow rotations. Simulations and experiments are presented to validate our methods.

Key words: Dynamic SPECT, least squares methods, compartment models, interface method.

I. Introduction

The goal of emission computed tomography is to reconstruct the three dimensional radioactivity distribution of a metabolically active tracer which has been injected in the body and absorbed by the organ of interest. The available projection data have been acquired by a rotating camera or by a fixed cylindrical array of detectors surrounding the patient.

While metabolic processes are always intrinsically dynamic, current clinical applications of SPECT are generally static. The reason is that in the presence of a significant change of activity during the scan (due to metabolism and/or wash-out), a rotating camera system will acquire *inconsistent data*, that is, projections corresponding to different dynamic states of the unknown source. Traditional reconstruction methods like filtered backprojection and EM-based methods could then no longer be used as they are not designed to account for dynamics, and if applied to inconsistent projections, produce serious artefacts in the reconstructed images.

Dynamic imaging is possible in PET and with ring SPECT instruments since in these cases a complete set of angular views may be scanned in sufficiently short time. The data acquired within each frame are then again consistent and may be inverted by static methods. Dynamics are finally accounted for by doing a series of static images. With a rotating triple head camera, one may mimick this situation by doing a series of *fast rotations*, allowing to scan a complete set of angular views in a short time during which the object may be assumed stationary, [13, 22]. However, this approach suffers from poor data statistics, requires specially equipped triple head systems capable of doing multiple 360^0 rotations, and fails for single and double head cameras.

Our present approach takes a completely different point of view. We propose a *dynamic* reconstruction method which is capable of processing inconsistent dynamic projection data. This becomes inevitable as soon as data may no longer be collected into consistent subgroups, and have to be treated *simultaneously*. As opposed to the above mentioned approaches via *successive static imaging*, our new approach tries to build the entire movie at a time.

The observation that a metabolized radiotracer could never behave entirely static is of course a commonplace. Nonetheless, the traditional point of view is to ignore its dynamic or to consider it a source of errors: blurr in reconstructed images, and even false diagnostics [17, 26, 18]. Tracers, therefore, were designed to *avoid* dynamics, and methods were proposed to eliminate dynamics by correcting data accordingly. With a new dynamic reconstruction method at hand, this point of view should change entirely, and using genuinely dynamic tracers should become attractive.

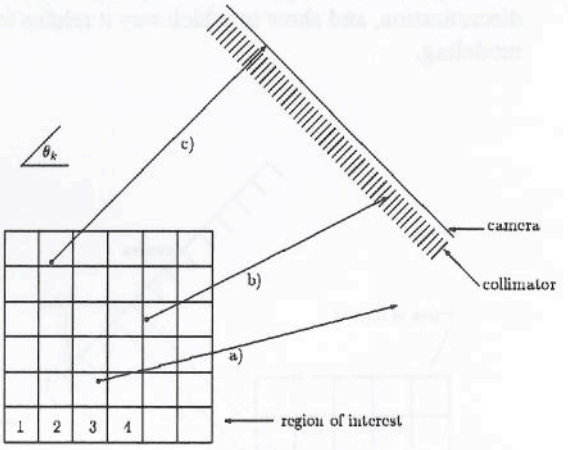

Figure 1. Photons radiating from the region of interest. a) misses the camera, b) is absorbed by the collimator, c) passes the collimator and hits the camera.

Similar to the situation in PET, one should then seek to combine *dynamic* information, currently available in planar imaging, with *spatial* information, presently obtained in static SPECT. Various kinetic processes may then be successfully assessed through SPECT protocols, with exciting new diagnostic possibilitites. As opposed to PET and ring SPECT cameras, which require a complicated and expensive setup, our new approach, compatible with single and double head

cameras available in most hospitals, is easier to realize as it uses the existing clinical SPECT data acquisistion protocols.

We observe that the dynamic point of view may even be advisable in situations (ring SPECT, PET) where successive static imaging *is* possible. Cutting into frames and treating as independent information what is actually highly correlated may appear unsatisfactory. An approach to *dynamic* PET reconstruction in this sense is presented e.g. in [9, 16].

For the sake of clarity, we mention a different source of dynamism which should not be mixed with our present theme: gated SPECT for the beating heart. Here dynamism is accounted for by collecting data in subgroups each considered static, and does not fall within the scope of tracer based dynamics.

The paper is organized as follows. Sections II – VI present and elaborate our method and some of its modifications. Sections VII – IX present a phantom experiments, and a clinical example.

As a result we will provide guidelines on (a) how to reconstruct images, and (b) how to estimate dynamic parameters related to metabolic processes. Hopefully, our approach will lead to new diagnostic methods based on SPECT and provide new insight into functional processes of the body.

II. Dynamic Model

In this section we briefly review the mathematical model defining the inverse problem of dynamic SPECT, discuss its discretization, and show in which way it relates to departmental modeling.

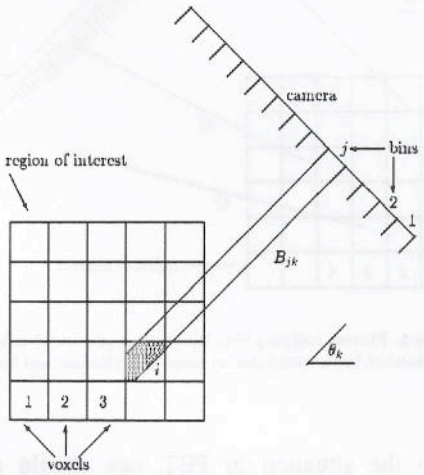

Figure 2. The coefficient c_{ijk} is the relative volume of voxel i lying within the beam B_{jk} connecting i and the receptor bin j during the camera position θ_k.

We shall make the assumption that the scatter contribution is ignored, or taken into account either by correcting data or by interpreting scatter as a source of noise. As shown in Appendix 1, the inverse problem may be decoupled into a series of dynamic reconstructions of 2D slices. In each slice, we encounter the nonlinear integral equation involving the *dynamic attenuated Radon transform*:

$$R[a,f](s,\omega) = \int_{-\infty}^{\infty} f(x,t)\cdot e^{-\int_x^{\infty} a(y)\,dy}\,dx = g(s,\omega,t), \qquad (1)$$

to be solved for the unknown variables f and a. Here $f(x,t)$ is the activity of the unknown source at position $x \in \mathbb{R}^2$ and time t, and $a(x)$ is the linear attenuation coefficient. Notice that the integrals in (1) are line integrals along the lines $L(s,\omega) = \{t\omega + s\omega^{\perp} : t \in \mathbb{R}\}$, where $\omega = (\cos\theta, \sin\theta)$, $\omega^{\perp} = (-\sin\theta, \cos\theta)$, and $g(s,\omega,t)$ represents the ideal data acquired along this line at time t.

Let us now consider the discretization of (1), choosing, exemplarily the case of a single head camera. Let the time domain be divided into S intervals of duration Δt, leading to a total acquisition time of $S\cdot\Delta t$. Let $t_k = (k-1)\Delta t$, so the kth stop is $[t_k, t_k+\Delta t]$ referenced t_k or simply k. We assume that during $[t_k, t_{k+1}]$, the activity of the source remains constant. Since a single head camera takes one position ω_k at a time t_k, we have $\omega_k = (\cos\theta_k, \sin\theta_k)$ with $\theta_k = (k-1)\Delta\theta$, and we are scanning a sector of $S\cdot\Delta\theta$ degrees.

Let the 1D cross-section of the camera be divided into M bins of size Δs, giving a cross-section of length $\ell = M\cdot\Delta s$. The data registered in bin j during the kth stop are

$$y_{jk} = \int_{s_j}^{s_j+\Delta s}\int_{t_k}^{t_k+\Delta t} g(s,\omega_k,t)\,dt\,ds. \qquad (2)$$

Integrating (1) using (2) leads to the set of equations

$$\int_{s_j}^{s_j+\Delta s}\int_{t_k}^{t_k+\Delta t}\int_{L(s,\omega_k)} f(x,t)\cdot e^{-\int_x^{x_1} a(y)\,dy}\,dx\,dt\,ds = y_{jk}. \qquad (3)$$

Choosing a finite basis representation for f and a:

$$f(x,t) = \sum_{i=1}^{N} f_i(t)\psi_i(x), \qquad a(x) = \sum_{i=1}^{N} a_i\psi_i(x)$$

for an orthogonal system $\psi_1,\dots,\psi_N$ and substituting into (3) leads to the linear system

$$\sum_{i=1}^{N}\int_{t_k}^{t_k+\Delta t} f_i(t)\,dt\int_{s_j}^{s_j+\Delta s}\int_{L(s,\omega_k)}\psi_i(x)\times e^{-\int_x^{x_1} a(y)\,dy}\,dx\,ds = y_{jk}. \qquad (4)$$

The unknown variables are

$$f_{ik} := \int_{t_k}^{t_k+\Delta t} f_i(t)\,dt,$$

while the matrix coefficients

$$c_{ijk}(a) := \int_{s_j}^{s_j+\Delta s} \int_{L(s,\omega_k)} \psi_i(x)\, e^{-\int_x^{x_1} a(y)\,dy}\, dx\, ds \quad (5)$$

depend on the attenuation coefficient $a(x)$. During the following, we shall represent equation (4) by the compact notation $C(a)f = y$, y denoting the measured MS data vector, f the unknown NS dynamic image vector, a the unknown attenuation coefficient, and $C(a) = \{c_{ijk}(a)\}$ the above linear tensor converted into a 2D matrix of size $MS \times NS$, by letting $c_{i'j'} = c_{ijk}$ with $i' = i + (k-1)N$, $j' = j + (k-1)M$.

The traditional choice for the basis functions is to divide the region of interest into quadratic pixel B_i, $i = 1, \ldots, N$ of size $\Delta x \times \Delta x$, and letting

$$\psi_i(x) = \frac{1}{\Delta x^2} \chi_{B_i}(x)$$

the characteristic function of the ith pixel scaled to 1. We shall adopt this choice here, but mention that at least in the static case, other bases have been tested.

It is instructive to see the meaning of the matrix coefficients in the unattenuated case $a(x) = 0$. Here the integral (5) simplifies to

$$\begin{aligned} c_{ijk}(0) &:= \int_{s_j}^{s_j+\Delta s} \int_{L(s,\omega_k)} \psi_i(x)\, dx\, ds \\ &= \frac{1}{\Delta x^2} \int_{s_j}^{s_j+\Delta s} \int_{L(s,\omega_k)\cap B_i} dx\, ds, \end{aligned}$$

which is just the surface of that part of pixel B_i lying in the strip S_{jk} connecting to bin j during the camera position k (see Figure 2), and scaled by the full surface of the pixel. This indicates in fact the sparsity pattern of $C(a) = \{c_{ijk}(a)\}$, which is the same for all possible attenuation maps $a(x)$. For instance, in a typical case with a 64×64 region of interest (ROI), a camera whose cross section size is equal to the size of an edge of the region of interest, and discretized into 64 bins, and finally on the basis of 64 views over 180^0, the matrix C is only .046% filled.

We proceed to observe that equation (4) is largely underdetermined. This may be seen by considering the above example, a ROI with 64×64 pixels, 64 bins per camera cross-section, and 64 stops, where we have 64^2 measured data points to fit a dynamic image with 64^3 degrees of freedom. The situation is less dramatic if double or triple head cameras are used, but equation (4) remain under fitted. On the more abstract level of equation (1), this is explained by the fact that for a single head camera, the ideal data are $g(s, \omega(t), t)$, with only one direction $\omega(t)$ scanned at time t. As a consequence, and in contrast with the static case, we have to provide additional information in order to invert (1).

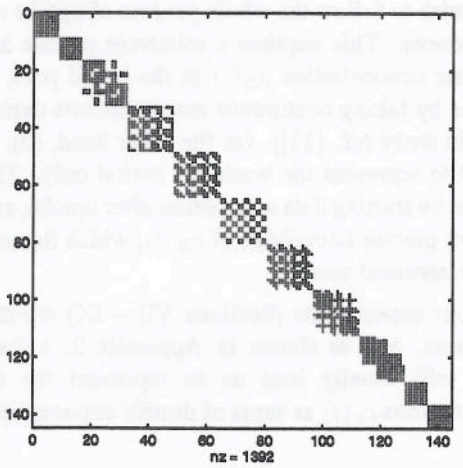

Figure 3. Sparsity pattern of the matrix $C^T C$ in case $S = 9$ stops, $M = 4$ bins, $N = 16$ pixels.

The missing information is provided by *compartemental modeling*, and we shall, very briefly, recall the essentials of this method.

The purpose of dynamic emission tomography being the understanding of the metabolic processes of the body, a radioactively labelled molecule (called the *tracer*) specifically selected for the organ of interest is injected in the body. The tracer molecule will undergo chemical reactions in the organ, and a usually simplified model of the complex chemical reaction will retain a certain number of chemical states referred to as *compartments*. Knowledge of the exchange rates between compartments is expected to reveal important information about the health of the organ.

Often the reactive scheme is modeled by a linear dynamical system involving the tracer concentrations $c_\nu(t)$ of the different compartments $\nu = 1, \ldots, P$ at time t. The tracer concentration in the blood compartment, $c_B(t)$, is often supposed to be known. The interplay between the compartments is then governed by a dynamical system

$$c'(t) = Kc(t) + c_B(t)p_0,$$

with a source term $c_B(t)p_0$, involving a contribution vector p_0, and a $P \times P$ coefficient matrix K representing reactive exchange rates k_{ij}. If the system matrix K is diagonalizable, the compartmental concentrations have an eigenfunction representation of the form

$$c_\nu(t) = \sum_{\kappa=1}^{P} \gamma_{\nu\kappa} e^{-\lambda_\kappa t} * c_B(t) \quad (6)$$

with $*$ denoting convolution. Here the unknown parameters $\gamma_{\nu\kappa}$ and λ_κ depend analytically on k_{ij}, p_0, and vice versa, so that knowledge of one set of parameters implies knowledge of the other.

For our experiments we concentrate on the 2-compartment model, $P = 2$. Two cases are possible. On one hand, (a), we might wish to follow the whole process of uptake *and* wash-out of the tracer. This requires a relatively precise knowledge of the tracer concentration $c_B(t)$ in the blood pool, obtained for instance by taking continuous measurements during the whole dynamic study (cf. [13]). On the other hand, (b), we might be content to represent the wash-out period only. This would be possible by starting data acquisition after uptake, and would not require a precise knowledge of $c_B(t)$, which in most cases may even be assumed zero.

In our experiments (Sections VII – IX) we shall consider both cases, and as shown in Appendix 2, a 2-compartment model will usually lead us to represent the compartment concentrations $c_\nu(t)$ as sums of double exponentials,

$$c_\nu(t) = \gamma_{\nu 1} e^{-\lambda_1 t} + \gamma_{\nu 2} e^{-\lambda_2 t} + \gamma_{\nu 3}. \tag{7}$$

How does compartmental modeling relate to tomography? Assuming that the reactive scheme may vary locally over the organ, the constants $\gamma_{\nu\kappa}$ and λ_κ are allowed to vary with the position x. Since all compartments contribute to radiation in the same way, the source term for the *localized 2-compartment model* is a sum of the local compartmental concentrations

$$f(x,t) = \gamma_1(x) e^{-\lambda_1(x)t} + \gamma_2(x) e^{-\lambda_2(x)t} + \gamma_3(x), \tag{8}$$

intended to capture situations where parts of the organ are unhealthy and show different reactive behavior.

III. Direct Methods

In this section we shall present a first approach to the inverse problem (1), (8) under the assumption that the attenuation map $a(x)$ is known. In our experiments, this is always the case since the attenuation map is either obtained through a transmission scan performed in parallel with the dynamic SPECT session (double head camera experiment, cf. [8, 7]), or may be mathematically estimated beforehand using emission data only (cf. [34, 23, 25]).

Discretizing the localized 2-compartment equation (8) and assuming that radioactivity is modeled by a Poisson law, we are lead to consider the *Nonlinear Poisson Model*:

$$(NPM) \quad \begin{array}{ll} \text{minimize} & \displaystyle\sum_{j=1}^{M}\sum_{k=1}^{S}\left(\sum_{i=1}^{N} c_{ijk} f_{ik} - y_{jk} \log\left(\sum_{i=1}^{N} c_{ijk} f_{ik}\right)\right) \\ \text{subject to} & f_{ik} = \gamma_{1i} e^{-\lambda_{1i} t_k} + \gamma_{2i} e^{-\lambda_{2i} t_k} + \gamma_{3i} \end{array}$$

Up to constant terms, the objective is the negative log-likelihood function for the joint Poisson law of the observed data. The model has been discussed at more details in [1].

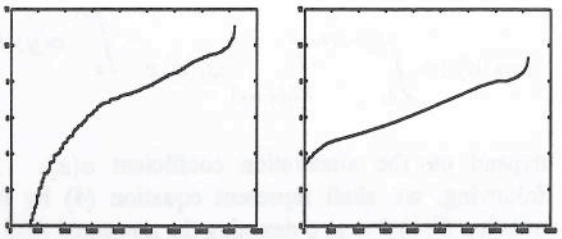

Figure 4. Plots of the singular values of C for different geometries. Both images show the case $N = 64^2$, $M = S = 64$ over 360^0. In the left hand plot, the camera cross-section equals the edge of the region of interest. In the right hand plot, the camera cross section has the length of the diagonal of the (square) region of interest.

A second approach, also examined in [1], and originally proposed in [17], replaces (NPM) by the following weighted *Nonlinear Least Squares* approach:

$$(NLS) \quad \begin{array}{ll} \text{minimize} & \displaystyle\sum_{j=1}^{M}\sum_{k=1}^{S} w_{jk}\left(\sum_{i=1}^{N} c_{ijk} f_{ik} - y_{jk}\right)^2 \\ \text{subject to} & f_{ik} = \gamma_{1i} e^{-\lambda_{1i} t_k} + \gamma_{2i} e^{-\lambda_{2i} t_k} + \gamma_{3i} \end{array}$$

Both (NPM) and (NLS) are nonlinear optimisation problems with $5N$ unknown variables (γ, λ), and a hidden constraint $f_{ik} \geq 0$ in (NPM). One may add regularizing terms to both objectives, as explained in Section IV and Appendix 3, and likewise introduce linear inequality constraints.

We implemented both methods using the limited memory BFGS code with bounds by Nocedal et al. [19, 4]. A Levenberg-Marquardt algorithm used in [17] could not be tuned to work satisfactory due to the size and high nonlinearity of the problem. With a careful adaption of the stopping criteria and a good initial guess, both algorithms may reconstruct a typical slice in 1 - 2 hours CPU, which is a little long for convenient clinical applications.

The difficulty of (NLS) may to some extent be understood from a mathematical analysis presented in [2]. The authors show that difficulties ought to be expected as soon as some of the eigenvalues λ_{1i} and λ_{2i} coalesce, but otherwise relate performance to the condition number of the matrix $C(a)$, which as we shall see is usually satisfactory (see Figure 4). An obvious drawback of both approaches is the large number of local minima, which renders performance highly dependent on the initial guess, and often produces aberrand solutions.

IV. Relaxation Methods

As a remedy to the algorithmic problems of (NPM) and (NLS), we propose a relaxation which temporarily abandons the constraint $f_{ik} = \gamma_{1i} e^{-\lambda_{1i} t_k} + \gamma_{2i} e^{-\lambda_{2i} t_k} + \gamma_{3i}$ imposed by the compartmental modeling. In order to present the idea, let us first consider the case (b), where only washout is represented, and the activity of the dynamic image decreases. We propose a

weighted *Linear Least Squares* problem

$$(LLS) \qquad \begin{array}{ll} \text{minimize} & \displaystyle\sum_{j=1}^{M}\sum_{k=1}^{S} w_{jk}\left(\sum_{i=1}^{N} c_{ijk} f_{ik} - y_{jk}\right)^2 \\ \text{subject to} & f_{i1} \geq f_{i2} \geq \ldots \geq f_{iS} \end{array}$$

where we have replaced the biexponential decay profiles by an arbitrarily decaying curve. This increases the number of variables dramatically, SN for (LLS), versus $5N$ in (NLS), but leads to a quadratic programming problem with a very convenient linear constraint structure. With a change of variables

$$f'_{ik} = f_{ik} - f_{i,k+1}, \tag{9}$$

(LLS) may be transformed in a quadratic program with box constraints.

If uptake and washout have to be represented, the constraint set has to be modified. In the renal study presented in Section V, we find a first guess for the peak activity at $k_{\max}$, and then set constraints of increasing-decreasing activity which allow the reconstruction to automatically choose a maximum at $k_{\max} \pm 1$. The constraint set is then

$$\begin{array}{l} 0 \leq f_{i1} \leq f_{i2} \leq \ldots \leq f_{i,k_{\max}-1}, \\ f_{i,k_{\max}+1} \geq \ldots \geq f_{iS} \geq 0, \\ f_{i,k_{\max}} \geq \frac{1}{2}(f_{i,k_{\max}-1} + f_{i,k_{\max}+1}), \end{array} \tag{10}$$

which allows the curves f_{ik} to select their peaks among the positions $k = k_{\max}-1, k_{\max}, k_{\max}+1$. The change of variables (9) again gives a quadratic program with box constraints.

Let us analyze the performance of (LLS). Writing $f = Tf'$ for the change of variables (9), the decreasing case (b) may be reformulated as

$$(LLS') \qquad \begin{array}{ll} \text{minimize} & \|CTf' - y\|^2 \\ \text{subject to} & f'_{ik} \geq 0. \end{array}$$

and correspondingly in the increasing-decreasing case (a) using the constraint set (10) in tandem with (9). Our implementation of (LLS') uses a method proposed by Moré and Toraldo [21], which extends the gradient projection method by the possibility to doing a conjugate gradient based minimization on a suitable face of the admissible set. A single outer iteration of the algorithm consists in doing gradient projection steps until a face has been identified worth doing a complete minimization, and the outer step ideally ends with the minimum on this face. Performance of the method therefore depends on (i) the speed of the cg-based minimization on the chosen faces, and (ii) the number of gradient projection steps needed before settling on a face.

Analyzing the cg-step is done along the usual lines. Fixing a face of the admissible polytope corresponds to fixing certain coordinates f'_{ik}. Given the current iterate f'_c, we obtain the new iterate $f'_+ = f'_c + \Delta f'$ by solving the problem

$$\begin{array}{ll} \text{minimize} & \|CT(f'_c + \Delta f') - y\|^2 \\ \text{subject to} & A_c \Delta f' = 0. \end{array}$$

Here A_c is the matrix fixing the coordinates corresponding to the chosen face, $A_c(f' + \Delta f') = A_c f'$. Letting Z a projector onto $\ker A_c$, and substituting $\Delta f' = Z(\delta f')$, with $\delta f'$ the reduced vector of free coordinates in $\Delta f'$, this is equivalent to solving the linear system

$$(Z^T T^T C^T C T Z)\delta f' = Z^T T^T C^T (y - CTf'), \tag{11}$$

and performance of the conjugate gradient step therefore depends on the condition number of the system matrix $S = Z^T T^T C^T C T Z$. Observe that since $C^T C$ is highly rank deficient, S is not regular and requires regularization, either by using $C^T C + \epsilon I$ instead of $C^T C$, or by regularizing S directly, $S_\epsilon = S + \epsilon I$.

The maximum eigenvalue of S is majorized by the maximum eigenvalue of $T^T C^T C T$, which in our typical example was calculated as $\lambda_{\max}(T^T C^T C T) \approx 1.5 \cdot 10^5$. The singular value distribution of C is in fact quite good, two typical cases are displayed in Figure 4. What appears more critical is the change of variables (9), which has $\text{cond}(T^T T) \approx 1686$. If the regularization $C^T C + \epsilon I$ with $\epsilon \approx 10$ is used, the usual pessimistic formula for the number of cg-iterations

$$\frac{\|\delta f'_m - \delta f'_*\|}{\|\delta f'_0 - \delta f'_*\|} \leq \frac{2(\kappa - 1)^m}{(\sqrt{\kappa}+1)^{2m} + (\sqrt{\kappa}-1)^{2m}}$$

($\kappa = \text{cond}(S_\epsilon)$, $\delta f'_*$ the solution of (11)), would indicate of the order of 50 cg-iterations to obtain a 30% error reduction. In practice, we usually do much better, which is due to the fact that the true system matrix S_ϵ is usually better conditionned than $T^T(C^T C + \epsilon I)T$, so that of the order of $10 - 50$ cg-iterations usually give satisfactory convergence on a face. We notice that as compared to a linear system, the constraint structure naturally complicates the situation. For instance, it is not of much help to have a preconditioner for $H_\epsilon = T^T(C^T C + \epsilon I)T$, although a way to include this information is discussed in [12]. In fact, the inverse of H_ϵ is readily calculated using the Sherwood-Morrison-Woodbury formula, but the cg-step requires preconditioning S_ϵ rather than H_ϵ.

The number of projection steps needed to find a suitable face is the second ingredient of good performance. In fact, if the algorithm needs too many gradient projection steps, the complexity will become exponential, and the approach will fail. Our analysis shows that the relative success of (LLS') is in fact based on a surprisingly small number of gradient projection steps. What may be prohibitive is the Tychonoff regularizing term $\epsilon\|f'\|^2$, since its contribution $-\epsilon f'$ to the negative gradient reflects the constraint structure at the current iterate, and may therefore prevent the algorithm from selecting a new (and better) face. We therefore do *not* Tychonoff regularize the objective function as a whole, but prefer an adapted regularization for the individual cg-steps, i.e., we prefer S_ϵ over H_ϵ.

For the typical slice, an (LLS) solution will be obtained with up to 6 - 20 outer iterations. A typical profile, plotting the number of cg-iterations and gradient projections per outer iteration is shown in Figure 5. The algorithm converges with typically between 2 and 10 minutes CPU for the typical slice.

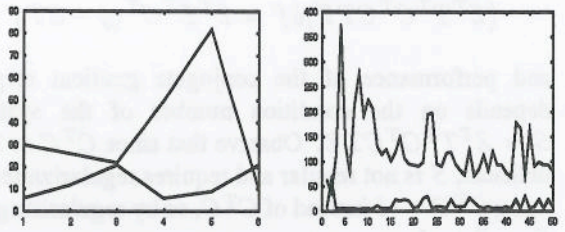

Figure 5. The diagrams show the performance of (LLS) for the increasing-decreasing model (10) (left) and the concave-convex model using second differences (12) (right). The upper curve shows the number of iterations per cg-step. The lower curve shows the number of gradient projection steps needed to settle on a face. Convergence was obtained after 6 outer iterations in the decreasing-increasing case (left), and 50 outer iterations in the concave-convex case (right).

A change of variables involving second differences

$$f''_{ik} = f'_{ik} - f'_{i,k+1} \tag{12}$$

may appear attractive when modeling an increasing-decreasing profile as in the renal SPECT experiment. Inspecting the planar imaging curve in Figure 7 shows that a concave-convex profile is expected. While first differences leave us with the delicate problem of locating the peak, a concave-convex curve would require locating the inflection point instead, which seems less error sensitive. However, the corresponding second difference matrix $f = T'f''$ is prohibitively badly conditioned, and we have not been able as yet to tune the method to converge in acceptable time.

V. Interface Methods

The solution f obtained from a relaxation method (LLS) does not have the doubly exponential form imposed by the underlying compartemental philosophy. We therefore fit the required exponential curves to the dynamic image f. This may be done on a pixel-by-pixel basis, or by drawing regions of interest and fitting exponentials to the corresponding dixels or their sum.

While aposteriori fitting will be briefly discussed in the subsequent section, we presently emphasize that the fit may *either* be the final result of the entire procedure, as is the case in the phantom experiment, *or* we may use the fitted biexponential curve $\hat{f}$ as a starting point to a new instance of (LLS) or $(NLS), (NPM)$. This new instance of (LLS) will usually add a penalty term of the form $K\|f - \hat{f}\|^2$ to the objective in order to bias the algorithm towards the previously obtained fit $\hat{f}$. Iterating back and forth a few times between the results f of the relaxation method, and the fitted curves $\hat{f}$ will usually improve the quality of the reconstruction. As (LLS) is surprisingly fast, several iterations back and forth are acceptable for a single slice, and this is what we refer to as *interface methods*. The user may intervene at the stages f and $\hat{f}$, doing visual checks and inspecting curves. On the other hand, the decision on whether an improved f has to be sought for could also be automatized.

This rises the question in which way and at what stage further prior information could be used. Instead of running (LLS) in its raw form, we use several prior steps to improve the quality of the reconstructed images.

A first step is data filtering, which due to the inconsistency of the projections is done in 2D. In [20] we analyzed the spectrum of the dynamic Radon transform, and proposed a 2D filter for the sinogram as a whole, using the theoretically expected bowtie shape.

As a second step, we run a static version of the EM-algorithm using the dynamic data. While FBP would usually fail quite badly for such data, EM often performs surprisingly well and reconstructs an *average* state of the dynamic source. This helps locating the object spatially, often gives the contour of the body, and provides first estimates of the attenuation map, if required. Using the averaged static image and the overall dynamic profile (estimated e.g. through the projection data or other prior knowledge), we create the initial iterate for the first instance of (LLS).

Thirdly, after a static fit or a preliminary raw (LLS) reconstruction, we use the localization of the source to find and include spatially regularizing terms in the (LLS) objective, and we use weights w_{jk} to reduce artefacts. As we have noticed, spatial regularization is of minor importance if the length $\sqrt{N}\Delta x$ of the edge of the ROI is adapted to the length ℓ of the camera cross-section. New ideas are needed, however, for regularization in time. In Appendix 3 we present a regularizer which tries to stabilize by minimizing the kinetic energy in the dynamic images f.

Finally, in the case of the increasing-decreasing model the user may, between two instances of (LLS), wish to modify the peak positions $k_{\max}$ of the individual dixels. This may be done if a reconstructed curve $f_{i\cdot}$ shows a large plateau around the originally chosen peak position, indicating that $k_{\max}$ should be shiftet to one side. This is for instance the case in the (LLS) reconstruction of the renal example, where the curves for the left kidney are too flat and indicate that the peak should be shifted to the right.

VI. Fitting Exponentials

Fitting data by a sum of exponentials in the least squares sense or other is well-known to be difficult computationally. Consequently, there is an abundance of statistical literature on the subject, and we have counted at least 10 different methods, some of them rather sophisticated, others of more adhoc style. We mention the references [32, 29, 28, 15] and the textbook [30] with a special chapter on compartmental modeling.

As far as applicability to our present situation is concerned, we have to distinguish two situations. If a fit to a single dynamic pixels or a sum of those (selected by drawing a ROI in the reconstructed image f) is required, practically any of these method could be used. We remark that the state of art of global optimization now even allows a search for the global optimal fit in acceptable time.

The picture changes if the exponential fit $\hat{f}$ is used to create the starting point to a new instance of (LLS) or another box. In the extreme case this would require fitting exponentials on a pixel-by-pixel basis, so has to be fast and reliable. In particular, methods which require visual inspection (like exponential peeling) could not be used. Since many of the output dixels from f may show strongly nonexponential profiles, the risk of obtaining aberrand parameters in $\hat{f}$ is high, and should be limited through the use of constraints. For instance, in the renal example we expect increasing-decreasing profiles similar to the ones shown in Figure 7, which could be assured by the program

$$(EF) \qquad \begin{array}{ll} \text{minimize} & \sum_{k=1}^{S} \left(\gamma_1 e^{-\lambda_1 t_k} + \gamma_2 e^{-\lambda_2 t_k} + \gamma_3 - f_{ik}\right)^2 \\ \text{subject to} & \lambda_1 \geq \lambda_2 \geq 0 \\ & \gamma_1 + \gamma_2 \geq 0,\ \gamma_2 \geq 0,\ \gamma_3 \geq 0. \end{array}$$

A method we have been applying successfully uses *slow dynamics* to stabilize: We first detect the peak activity positon of the ith data dixel $f_{i\cdot}$, say $k_{\max}$, and then fit a monoexponential $\gamma_2 e^{-\lambda_2 t_k} + \gamma_3'$ to the tail $f_{i,k_{\max}}, \ldots, f_{iS}$ of the data, assuming that the slower dynamic will prevail in the later positions. Subtracting the result from the data, we fit another monoexponential $\gamma_1 e^{-\lambda_1 t_k} + \gamma_3''$ to the residue, obtaining with $\gamma_3 = \gamma_3' + \gamma_3''$ a fit of the sought for form (8). We may now either use the parameters $\tilde{f}$ so obtained directly as $\hat{f}$, or obtain a fit $\hat{f}$ using $\tilde{f}$ as starting value for program (EF).

We finally notice that an idea often used in compartmental modeling consists in successively increasing the number of exponentials used to fit the data until certain criteria indicate saturation (cf. [30, 14]). In the absence of theoretical knowledge, this may identify the number P of discernable compartments. We doubt that this strategy will work in our present context since we often face profiles f which hardly resemble sums of exponentials, and would often lead us to overestimate the number P of compartments.

VII. Experiment 1

Our first experiment uses projection data generated by a dynamic heart-in-thorax phantom [5] built at the Vancouver Hospital. Initially all parts of the phantom heart are filled with activity. Uniform water flow through each container dilutes and washes out these activities. This produces single exponential dynamic activity changes determined by the speed of the water flow. The study shown in Figure 6 uses 4 similar containers (one of them shown in top line right) with decreasing activities of different half lives (2, 4 , 6 minutes) acquired over 12 minutes. The 17ml containers each equipped with a mixing propeller are initially filled with Tc-99m with activity levels ranging from 70MBq to 40MBq. A Siemens Multispect-3 (MS3) triple head camera with low energy ultra high resolution (LEUHR) collimator was used. The initial positions of the heads are 0^0, 120^0 and 240^0, and each head rotated over 180^0 with 64 stops, collecting 64 data per camera cross section and stop. Letting the length of the camera cross section 40cm, the region of interest was chosen as 35×35cm. The data acquired by the first of the camera heads were used to simulate a single head camera. Figure 6 (first line, left) shows the sinogram of the first head. Line 2 shows a (LLS) reconstruction of a slice displayed at times 0, 3 and 9 minutes. The first image shows serious streaking artifacts towards the 0^0 position of the camera. To enhance the image, a region of support surrounding the four bottles was automatically generated from the last of the 64 images reconstructed by (LLS) (line 2). (LLS) was then restarted using the $0-1$ image as apriori information. Line 3 shows the result of a restart of (LLS) which used an initial estimate $f^{(0)}$ obtained by scaling the $0-1$ image to capture the energy level of the raw restoration and then generating replica with activity decreasing in time. The (LLS) reconstruction shown in line 4 uses the prior $f^{(0)}$ obtained by truncating the result of line 2 outside the region of support. Both restarts of (LLS) were using a penalty term $K\|f - f^{(0)}\|^2$ to stabilize towards the previously obtained estimate $f^{(0)}$. In order to test the quality of the single head images, a (LLS) reconstruction using the data acquired by the three heads simultaneously is shown at the same instants in line 5. Notice that attenuation was ignored in this experiment, and data were not filtered prior to inversion.

	Sinogram	LLS	
		1 head	3 head
Half-life (min)	1.95	2.95	2.15
Initial activity (counts)		7.96	15.45

	NLS monoexp		NLS biexp	
	1 head	3 head	1 head	3 head
Half-life (min)	2.27	2.09	2.46	2.32
Initial activity (counts)	13.32	15.90	11.07	14.18

Table 1. The half life of the container with the fastest wash-out (2 minutes) (rightmost in Figure 6) was estimated by different methods. Reconstructions based on the data acquired by one camera head tend to overestimate the half life due to the missing initial activity blurred into the streaking artifacts.

In order to validate the dynamic parameters, we directly estimated the half lives of the four bottles by fitting lines to the log-plots of the dixels in each bottle. A quality check is possible on the basis of the triple head reconstruction, which is apparently almost perfect, and knowledge of the physical

experiment itself. Observe that the single head reconstructions tend to overestimate the half lives of the bottles due to the missing activity in the first views blurred into the streaking artefacts. With the help of our interface technique, this effect could be reduced considerably.

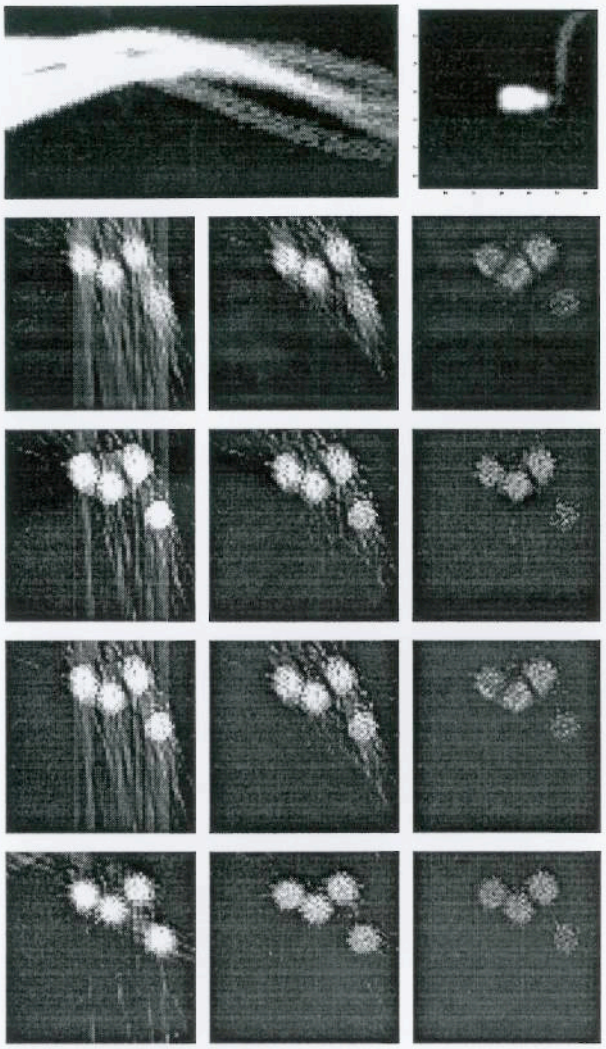

Figure 6. The first line (left) shows the sinogram of the first camera head. Line 2 shows the raw (LLS) reconstruction at 0, 3 and 9 minutes. In order to reduce the typical streaking artifacts visible in the first view, line 2 was used to automatically generate a 0 – 1 image identifying a region of support of the object. The latter served as a priori to the (LLS) reconstructions on lines 3 and 4. Line 3 chooses as initial $f^{(0)}$ the scaled 0 – 1 image with activity decreasing in time, while line 4 chooses as initial guess the result of line 2 truncated outside the region of support. In both cases, a penalty term $K\|f - f^{(0)}\|^2$ is used to bias towards the prior. The last line shows the reconstruction obtained from the three heads simultaneously.

VIII. Experiment 2

In this section we describe a clinical study performed at the Vancouver Hospital. A testperson was administered a dose of 15ml i.v. of the dynamic renal tracer Tc-99mMAG3. Two minutes after injection, we started the SPECT session with a Ecam double head camera. The camera was equipped with a gadolinium emission source in order to obtain a transmission scan parallel to SPECT. The test persion was scanned in prone position, the camera heads initially at 0^0 and 90^0. Each head rotated over 90^0, taking 64 stops each of 10 seconds duration, so both heads together scanned a 180^0 sector. The total acquisition time was 12 minutes 48 seconds, with a dead time of 2 seconds per position.

The results are shown in Figure 7. The first line shows the sinogram of the two heads. In order to emphasize the dynamic nature of the experiment, we prefer not to arrange, as one would do in the static case, the data from the two heads to obtain a single sinogram over 180^0. The attenuation map (line 2, right) was reconstructed on a 128×128 grid and used to build the matrix $C(a)$. It also served to reduce the ROI to a smaller size 86×86.

After estimating the peak position at $k_{\max} = 8$ from the acquisition protocol, (LLS) with constraints (10) was run, and the reconstruction f was used to automatically generate two masks (line 2) locating the left and right kidney. Line 3 displays those dixels from f which are inside the masked regions (right kidney to the left).

Using the method from Section VI we fitted biexponentials (8) to the output f of (LLS). To ensure the increasing decreasing profile, we used the constraints

$$\gamma_{1i} + \gamma_{2i} \geq 0,\ \gamma_{2i} \geq 0,\ \gamma_{3i} \geq 0,\ \lambda_{1i} \geq \lambda_{2i} \geq 0.$$

The fit $\hat{f}$ was now used to run (NLS) and to re-run (LLS) with inital iterate $\hat{f}$. The result for (NLS) at times 2, 6 and 12 minutes is displayed in line 4, and the dixels belonging to the masked regions are shown in line 5. Line 6 shows the result of a restart of (LLS) with $\hat{f}$ as input, and line 7 shows the corresponding dixels. Finally, line 8 shows the result of adapting a biexponential to the sum plot of both kidney. Since only two curves had to be fitted, we calculated the global minima for the problem (EF).

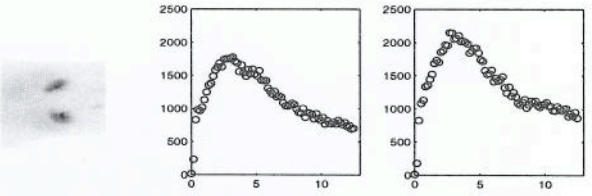

Figure 7. Results of conventional planar scan with the dynamic tracer TC-99mMAG3 used to assess the glomerular filtration rate (GFR). The time scale is in minutes.

In order to validate the reconstruction, a planar dynamic renal scan using 10ml of Tc-99mMAG3 was performed prior to the dynamic SPECT session, and revealed the form of the expected dynamic profiles (Figure 7). The curves on line 7 of Figure 8 should be compared to those in Figure 7.

Our present acquisition protocol may not be optimal as far as the number of stops are concerned. In fact, in static scans with a double head camera, 32 stops are often considered sufficient. According to our mathematical analysis [20], 64

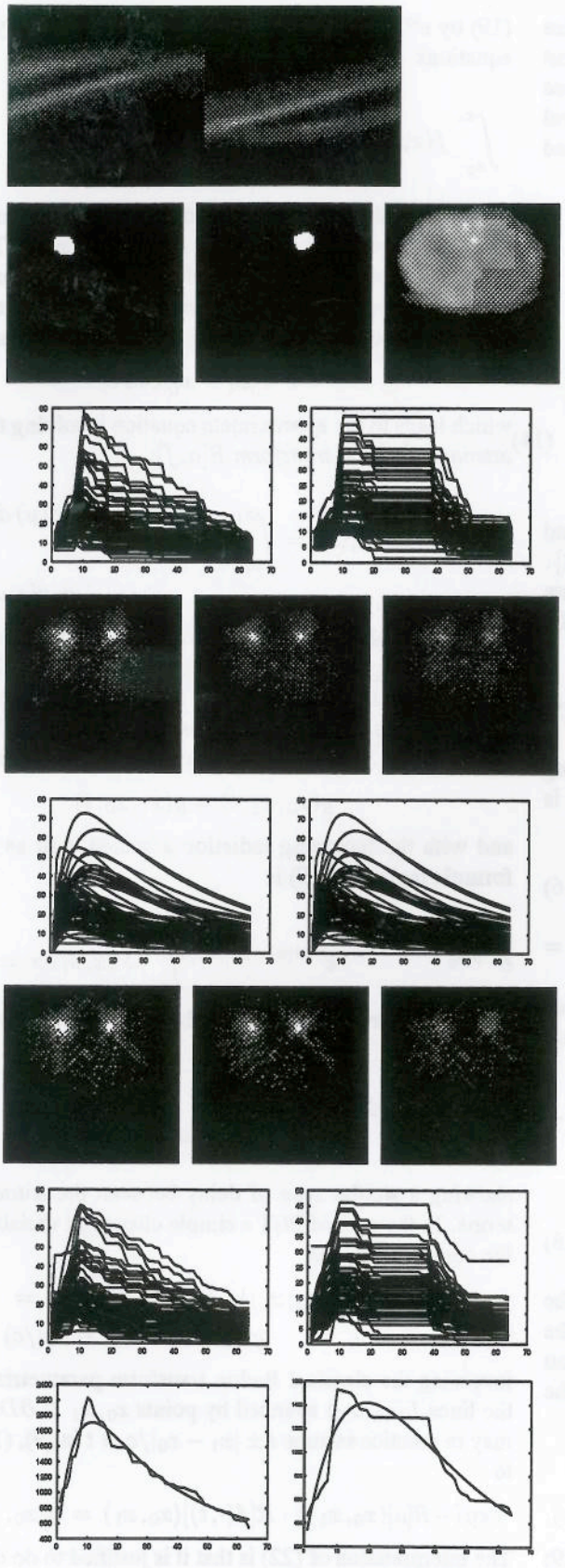

Figure 8. Results of a clinical dynamic SPECT experiment with the dynamic tracer TC-99mMAG3.

stops seem appropriate, but a future clinical test should provide more evidence on this quest. As a second point, we remark that the dosage was chosen rather conservatively, and a slightly higher dose might produce more reliable results.

IX. Conclusion

We have presented several nonlinear programming based approaches to solve the dynamic SPECT reconstruction problem. As direct fitting of the Radon transform of a biexponential to the dynamic projection data, (NLS), turned out difficult computationally. We proposed a relaxation scheme based on a convex quadratic program with box constraints, (LLS), which we combined with aposteriori fitting of biexponentials and an interface technique using several re-starts of (LLS). The relaxed approach is faster and robust. Using a phantom experiment and a clinical test, we validated our approach and showed that it reconstructs dynamic parameters even with a single head camera.

While a conclusive comparison between the various methods requires further testing, the approach we have chosen is promising, in particular if prior information is used to adapt it to a specific situation. We have shown that dynamic reconstruction may and should be based on *slow rotations*.

In the clinical test we proposed a rather high number of stops (64 per camera head on a 90^0 sector for each head) in order to account for the fast dynamics during uptake. Future testing might show that a smaller number of stops is sufficient. While our cameras only allow for stops of equal length, an optimal protocol might require more flexible stops of individual duration.

X. Appendix 1 - Transport Model

Dynamic emission tomography is described by the dynamic photon transport equation (cf. [10, Vol. I, Section 5])

$$\frac{1}{c}\frac{\partial}{\partial t}u(x,\omega,E,t) + \omega\cdot\nabla u(x,\omega,E,t) + a(x,E)u(x,\omega,E,t) = \int_0^\infty \int_{\mathbb{S}^2} b(x,E',E,\omega',\omega)u(x,\omega',E',t)\,d\omega'\,dE' + f(x,E,t) \quad (1$$

Here $u(x,\omega,E,t)$ is the density of the angular transport of photons at position x and time t in direction $\omega \in \mathbb{S}^2$, and with energy E, c is the speed of light, $a(x,E)$ is the linear attenuation coefficient, $b(x,E,E',\omega,\omega')$ the scattering kernel (both unknown), and $f(x,E,t)$ is the unknown radioactive source we wish to estimate. The energy of photons used in nuclear medicine is monochromatic, so ideally $f(x,E,t) = f(x,t)\,\delta(E-E_0)$ for a fixed energy level E_0. (For example, $E_0 = 140$keV for ^{99}Tc used in SPECT, and $E_0 = 511$keV in PET).

The 3D model (13) is certainly required if scatter is taken into account. However, it is usually justified to ignore the scatter contribution or rather, to interpret it as a source of noise in the

data. This allows us to break the 3D reconstruction into a series of 2D reconstructions, and we may then restrict the transport model to the 2D case. With $b \equiv 0$, the energy dependence of transport could then be restricted to the fixed energy level E_0. Integrating (13) over all energy levels using the averaged angular transport

$$u(x,\omega,t) = \int_0^\infty u(x,\omega,E,t)\,dE$$

leads to the simplified equation in $u(x,\omega,t)$

$$\frac{1}{c}\frac{\partial}{\partial t}u(x,\omega,t) + \omega\cdot\nabla u(x,\omega,t) + a(x)\,u(x,\omega,t) = f(x,t) \tag{14}$$

with $\omega \in \mathbb{S}^1$, $x \in \mathbb{R}^2$, $t \geq 0$.

As usual, we parametrize lines by $s \in \mathbb{R}$, and $\omega = (\cos\theta, \sin\theta) \in \mathbb{S}^1$, letting $L(s,\omega) = \{s\omega^\perp + t\omega : t \in \mathbb{R}\}$. Suppose the unknown source and attenuation coefficient are zero outside the unit disk D. Then the measured data may be understood as boundary information on D. Indeed,

$$u(x_0,\omega,t) = 0 \qquad \text{for } \nu_{x_0}\cdot\omega \leq 0, \quad x_0 \in \partial D \tag{15}$$

(ν_x = outer unit normal to D), i.e., there is no incoming radiation. And further, the outgoing radioactive transport is known:

$$u(x_1,\omega,t) =: g(s,\omega,t) \quad \text{for } \nu_{x_1}\cdot\omega \geq 0, \quad x_1 \in \partial D. \tag{16}$$

Here $L(s,\omega)\cap D = [x_0,x_1]$, and we call $x_0 = x_0(s,\omega), x_1 = x_1(s,\omega)$ the entry and exit points.

Assuming that the source $f(x,t)$ and data $g(s,\omega,t)$ decay sufficiently fast as $t \to \infty$ we may Fourier transform equation (14). This leads to the family of equations

$$\omega\cdot\nabla U(x,\omega,\sigma) + (a(x) + i\sigma/c)U(x,\omega,\sigma) = F(x,\sigma) \tag{17}$$

with boundary information

$$U(x_0,\omega,\sigma) = 0, \qquad U(x_1,\omega,\sigma) = G(s,\omega,\sigma). \tag{18}$$

Here capital letters refer to the Fourier transforms of the corresponding lower case functions, and σ stands for the Fourier domain variable. Integrating equation (4) using (5) on each segment $L(s,\omega)\cap D = [x_0,x_1]$ separately leads to the formula

$$\int_{x_0}^{x_1} F(x,\sigma)\cdot e^{-i\sigma|x_1-x|/c}\cdot e^{-\int_x^{x_1} a(y)\,dy}\,dx = G(s,\omega,\sigma), \tag{19}$$

which is a Fourier domain counterpart of the known integral equation obtained in the case of stationary SPECT based on the attenuated Radon transform (cf. [24, 23, 25]). Multiplying (19) by $e^{i\sigma t}$, Fourier inversion then gives the family of integral equations

$$\int_{x_0}^{x_1} f(x,t-|x_1-x|/c)\cdot e^{-\int_x^{x_1} a(y)\,dy}\,dx = g(s,\omega,t), \tag{20}$$

exhibiting a delay between the data acquired at time t and the source terms considered at times $t-|x_1-x|/c$. The method of characteristics (cf. [10]) would of course have produced the same result without using the Fourier transform. Since photons travel with the speed of light, we may in practice assume

$$t - |x_1 - x|/c \approx t,$$

which leads to the approximate equation involving the *dynamic attenuated Radon transform* $R[a,f]$:

$$R[a,f(\cdot,t)](s,\omega) := \int_{x_0}^{x_1} f(x,t)\cdot e^{-\int_x^{x_1} a(y)\,dy}\,dx = g(s,\omega,t). \tag{21}$$

For completeness, let us consider the situation in PET. Assuming again that the relevant information is captured by the disk D, we are led to use the PET-geometry which parameterizes the lines in the plane via the entry and exit points x_0, x_1 on ∂D. The boundary information being symmetric

$$g(x_0,x_1,t) = g(x_1,x_0,t),$$

and with the incoming radiation assumed zero as before, the formula replacing (19) is

$$e^{-\int_{x_0}^{x_1} a(y)\,dy}\cdot e^{-is|x_1-x_0|/c}\cdot\int_{x_0}^{x_1} F(x,s)\,dx = G(x_0,x_1,s),$$

and Fourier inversion provides the following family of integral equations

$$e^{-\int_{x_0}^{x_1} a(y)\,dy}\cdot\int_{x_0}^{x_1} f(x,t-|x_1-x_0|/c)\,dx = g(x_0,x_1,t),$$

showing a similar type of delay between the source and data terms. In the case of PET a simple change of variables leads to the compact formula

$$\exp\{-R[a](x_0,x_1)\}\cdot R[f(\cdot,t)](x_0,x_1) = g(x_0,x_1,t+|x_1-x_0|/c)$$

involving the classical Radon transform parametrized through the lines $L(x_0,x_1)$ spanned by points $x_0, x_1 \in \partial D$. Again we may in practice assume $t \pm |x_1-x_0|/c \approx t$ in (9), (10), leading to

$$\exp\{-R[a](x_0,x_1)\}\cdot R[f(\cdot,t)](x_0,x_1) = g(x_0,x_1,t) \tag{22}$$

The interpretation of (22) is that it is justified to do dynamics in PET simply by performing a series of static images, as proposed already in the basic reference for probabilistic approaches to PET [33].

XI. Appendix 2 - Compartment Model

In this section we exemplarily discuss a 2-compartment model for the renal example.

We assume that tissue is represented by two compartments with concentrations c_1, c_2. These represent chemical as well as physical states, so activity (in each position) is the sum of both contributions: $f(t) = \theta c_1(t) + (1-\theta)c_2(t)$, with another parameter $0 \leq \theta \leq 1$ controlling the local weighing between both compounds.

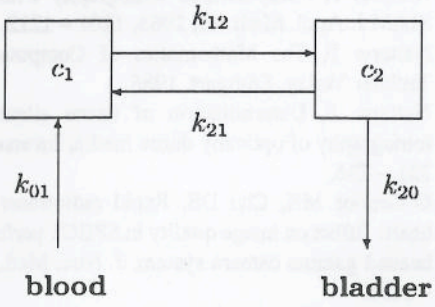

Figure 9. Two compartment model for the tracer TC-99mMAG3 in kidney. We assume that tracer in compartment 1 is stable, while molecules in compartment 2 are evacuated into the bladder at rate k_{20}.

The dynamical system describing this compartemnt model is

$$\begin{aligned} c_1' &= -k_{12}c_1 + k_{21}c_2 + k_{01}c_B \\ c_2' &= k_{12}c_1 - (k_{21}+k_{20})c_2 \end{aligned}$$

Assuming for simplicity that the input function c_B from the blood pool is constant during the scan, the solutions are of the biexponential form (7), and hence f is of the form (8).

As is readily verified from the equations, it will often be difficult or even impossible to assess the exchange rates k_{ij} by knowledge of the decay curves 8. For instance, if the mediation parameter is $\theta = .5$, that is, if both compartments contribute identically, the constants k_{12} and k_{21} cancel in the sum $f = c_1 + c_2$ and could not be assessed through knowledge of f.

Of course the model may be sophisticated by assuming more elaborate input functions $c_B(t)$ varying in time. A natural candidate would be c_B a constant value for a short time, and $c_B = 0$ afterwards, with another parameter governing the switch.

XII. Appendix 3 - Dynamic Regularizer

Let us now consider a heuristic leading to a regularizer in time. Consider Experiment 1, where we generated dynamics by diluting activity in the containers through water flow. Assuming that the container of volume V is initially filled with activity $f(0)$, and that washout is caused by water flow at rate $R(t)$, the activity $f(t)$ at time t is

$$f(t) = f(0)\, e^{-\int_0^t \frac{R(\tau)}{V}\, d\tau}$$

if the mixture between pure and radioactive water is perfect. Discretizing at times $t_k = (k-1)\Delta t$, and writing $f_k = f(t_k)$, $R_k = R(t_k)$, we have

$$-\frac{R_k \Delta t}{V} = \frac{f_{k+1} - f_k}{f_k}.$$

Assuming that the container is cylindrical, the flow rate is proportional to the speed of water flow, and the kinetic energy of the radioactive part of the flow at time t_k is

$$E_{\text{kin}} \propto f_k R_k^2 \propto \frac{(f_{k+1} - f_k)^2}{f_k},$$

regarding that activity is proportional to mass. As we can see, a strong difference in the activity levels f_{k+1} and f_k, according to the above model, must be caused by a high flow rate R_k, leading to a high kinetic energy E_{kin}. We therefore propose to include a penalty term

$$\alpha \sum_{i=1}^{N} \sum_{k=1}^{S-1} \frac{(f_{i,k+1} - f_{ik})^2}{f_{ik}}. \tag{23}$$

in the objective of (NLS), representing a integrated kinetic energy contribution from all dixels. Ideally, this relies on assuming that every pixel behaves like a small container of the above type. Minimizing kinetic energy will help to avoid irregular dynamic behavior and smoothen the output dixels.

As (23) is not a quadratic, it is not compatible with (LLS). Therefore, if a prior guess $\hat{f}$ is known, or if the interface technique is used, and the previous aposteriori fit $\hat{f}$ is available, we propose to use the regularizer

$$\alpha \sum_{i=1}^{N} \sum_{k=1}^{S-1} \frac{(f_{i,k+1} - f_{ik})^2}{\hat{f}_{ik}}$$

instead. We apply the same regularizer to curves with increasing activity.

Handling the penalty parameter α is based on the following heuristic. Let the random variable $(Cf)_{jk}$ have expected value y_{jk} and variance σ_{jk}. Then according to the law of large numbers,

$$\text{Var}\left(\sum_{j=1}^{M} \sum_{k=1}^{S} \frac{(Cf - y)_{jk}}{\sigma_{jk}} \right) = MS.$$

Assuming that the data y_{jk} are Poisson distributed, we are led to assume $\sigma_{jk}^2 = \text{Var}(y_{jk}) = y_{jk}$, and adopting the weights $w_{jk} = \sigma_{jk}^{-2} = y_{jk}^{-1}$ to tune the algorithm so that at the optimal solution f,

$$\sum_{j=1}^{M} \sum_{k=1}^{S} w_{jk} \left(\sum_{i=1}^{N} c_{ijk} f_{ik} - y_{jk} \right)^2 \approx MS.$$

Parameter value α which suit this heuristic are found experimentally, as no explicit formula is available.

XIII. References

[1] Bauschke HH, Noll D, Celler A, Borwein JM, An EM-algorithm for dynamic SPEC tomography, CECM Research Report 97-092, submitted to IEEE Trans. Med. Imag.

[2] Borwein JM, Sun W, The stability analysis of dynamic SPECT systems, Numerische Mathematik 77, 1997, 283 – 298.

[3] Buck A, Westera G, vonSchulthess GK, Burger C, Modeling alternatives for cerebral carbon-11-iomazenil kinetics, J. Nuclear Med. 37, 1996, 699 – 705.

[4] Byrd RH, Lu P, Nocedal J, Zhu C, A limited memory algorithm for bound constrained optimization, SIAM J. on Scientific Computing 16, 1996, 1190 – 1208.

[5] Celler A, Farncombe T, Harrop R, Lyster D, Dynamic heart-in-thorax phantom for functional SPECT, to appear.

[6] Celler A, Farncombe T, Harrop R, Noll D, Maeght J, Lyster D, Three approaches to dynamic SPECT imaging, to appear.

[7] Celler A, Sitek A, Harrop R, Reconstruction of multiple line source attenuation maps. In: 1996 IEEE Nuclear Science Symposium Conference Record, pp. 1420 – 1424, November 1996.

[8] Celler A, Sitek A, Stoub E, Lyster D, Dykstra C, Worsley D, Fung A, Development of a multiple line source attenuation array for SPECT transmission scans. J. Nuclear Medicine 38, 1997, 215ff.

[9] Chen K, Huang SC, Feng D, New estimation methods that directly use the time accumulated counts in the input function in quantitative dynamic PET studies, Phys. Med. Biol. 39, 1994, 2073 – 2090.

[10] Dautrey R, Lions JL, Analyse mathématique et calcul numérique, tome 9, Masson, Paris 1984.

[11] Farncombe T, Celler A, Noll D, Dynamic SPECT: a review of techniques for the determination of physiological kinetic rates, to appear.

[12] Gould NIM, Hribar ME, Nocedal J, On the solution of equality constrained quadratic programming problems arising in optimisation.

[13] Gullberg GT, Huesman RH, Ross SG, Di Bella EVR, Zeng GL, Reutter BW, Christian PE, Foresti SA, Dynamic cardiac single photon emission computed tomography, In: Nuclear Cardiology: State of the Art and Future Directions. Mosby-Year Book Inc., Philadelphia, PA. In press.

[14] Gjedde A, Compartemental Analysis. In: Principles of Nuclear Medicine, 2nd edition, eds Wagner HNJr, Szabo Z, Buchanan JW. Saunders, Philadelphia, pp. 451 – 461.

[15] Kammler DW, Least squares approximation of completely monotonic functions by sums of exponentials, SIAM J. Numerical Anal. 16, 1979, 801 – 818.

[16] Kao CM, Yap JT, Mukherjee J, Cooper M, Chen CT, An image reconstruction method for dynamic PET, IEEE NSS/MIC 1995 Conference Record.

[17] Limber MA, Limber MN, Celler A, Barney JS, Borwein JM, Direct reconstruction of functional parameters for dynamic SPECT, IEEE Trans. Nuclear Sciences 42, 1995, 1249 – 1256.

[18] Links JM, Frank TL, Becker LC, Effect of differential tracer washout during SPECT acquisition, Journal of Nuclear Medicine vol 32(12) pp 2253-2257, 1991.

[19] Liu DC, Nocedal J, On the limited memory BFGS method for large scale optimization problems, Mathematical Programming 45, 1989, 503 – 528.

[20] Maeght J, Noll D, Resolution in dynamic emission tomography.

[21] Moré J, Toraldo G, On the solution of large quadratic programming problems with bound constraints, SIAM J. Optimization 1, 1991, 93 – 113.

[22] Nakajima K, Taki J, Bunko H, Matsudaira M, Muramori A, Matsunari I, Hisada K, Ichihara T, Dynamic acquisition with a three-headed SPECT system: application of Technetium 99m-SQ30217 myocardial imaging, J. Nuclear Medicine 32, 1991, 1273 – 1277.

[23] Natterer F, Computerized tomography with unknown sources, SIAM J. Appl. Math. 43, 1983, 1201 – 1212.

[24] Natterer F, The Mathematics of Computerized Tomography, Teubner Verlag, Stuttgart, 1986.

[25] Natterer F, Determination of tissue attenuation in emission tomography of optically dense media, Inverse Problems 9, 1993, 731 – 736.

[26] O'Connor MK, Cho DS, Rapid radiotracer washout from the heart: Effect on image quality in SPECT performed with a single-headed gamma camera system, J. Nuc. Med., 33(6), 1992, 1146 – 1151.

[27] Oppenheim BE, Krepshaw JD, Dynamic hepatobiliary SPECT: a method for tomography of a changing radioactivity distribution, J. Nuclear Medicine 29, 1988, 98 – 102.

[28] Osborne MR, Smythe GK, A modified prony algorithm for exponential function fitting, SIAM J. Sci. Comput. 16, 1995, 119 – 138.

[29] Ruhe A, Fitting empirical data by positive sums of exponentials, SIAM J. Sci. Stat. Comp. 1, 1980, 481 – 498.

[30] Seber GAF, Wild, CJ, Nonlinear Regression, Wiley and Sons, 1988.

[31] van den Hoff J, Burchert W, Wolpers HG, Meyer GJ, Hundshagen H, A kinetic model for cardiac PET with [1-Carbon-11]-acetate, J. Nuclear Medicine 37, 1996, 521 – 529.

[32] Varah, JM, On fitting exponentials by nonlinear least squares, SIAM J. Sci. Stat. Comput. 6, 1985, 30 – 44.

[33] Vardi Y, Shepp LA, Kaufman L, A statistical model for Positron Emission Tomography, J. Amer. Stat. Assoc. 80, 1985, 8 – 20.

[34] Welch A, Clark R, Natterer F, Gullberg GT, Toward accurate attenuation correction in SPECT without transmission measurements, IEEE Trans. Med. Imag., 16(5), 1997, 532 – 541.

[35] Wells RG, Celler A, Harrop R, Analytic calculation of photon distribution in SPECT projections, IEEE Trans. Nuclear Sci.